Input torque balancing using a cam-based centrifugal pendulum: design optimization and robustness

B. Demeulenaere[*], P. Spaepen, J. De Schutter

Department of Mechanical Engineering, Katholieke Universiteit Leuven, Celestijnenlaan 300B, B-3001 Heverlee, Belgium

Abstract

In a companion paper (Input torque balancing using a cam-based centrifugal pendulum: design procedure and example, J. Sound Vib.), the cam-based centrifugal pendulum (CBCP) was introduced as a simple, cam-based, input torque balancing mechanism. The differential equation that governs the CBCP cam design was derived and a methodology for solving it was developed. Furthermore, in a design example, the CBCP was applied to balance the input torque of a high-speed cam-follower mechanism, driving the sley of a weaving loom. The present paper firstly shows how the design parameters for this particular design example can be optimized, so as to obtain a compact and technologically feasible mechanism. The formulation of the optimization problem is based on a parameterization of the CBCP rotor and coupler shape. Because of its nonconvex nature, the optimization problem is solved using a multi-start sequential quadratic programming (SQP) approach. A design chart, based on an exhaustive analysis, is introduced which (i) allows the designer to perform the design optimization in a quick and approximative way, and (ii) gives considerable insight into the behavior of the SQP-algorithm. Secondly, the CBCP is applied to an industrial case study, that is, a weaving loom. The robustness of the CBCP is illustrated by showing that input torque balancing solely the sley movement enhances the overall dynamic machine behavior, despite the presence of the non-balanced shed motion. A particular contribution of this part is the determination of the weaving loom regime behavior in the frequency domain, an approach which is believed to be novel in mechanism literature.
© 2004 Elsevier Ltd. All rights reserved.

Nomenclature

t	time (s)
$(.)$	first derivative w.r.t. time t
$(..)$	second derivative w.r.t. time t
T	period of motion (s)
L_r	half of rotor length (m)
L_c	coupler (pendulum) length (m)
R_b	rolling body radius (m)
J_r	rotor centroidal moment of inertia $(\mathrm{kg\,m^2})$
m_c, J_c	coupler mass (kg) and centroidal moment of inertia $(\mathrm{kg\,m^2})$
m_b, J_b	rolling body mass (kg) and centroidal moment of inertia $(\mathrm{kg\,m^2})$
X_c	location of the coupler center of mass along the line o_2–o_3 (m)
o_i	points defined in Fig. 1 ($i = \{1, 2, 2', 3, 3'\}$) and Fig. 3 ($i = \{2a, 2b, 2c, 3a, 3b\}$)
$g(t)$	rotor rotation angle w.r.t. X-axis (rad)
$q(t)$	coupler rotation angle w.r.t. X-axis (rad)
$s(t)$	$\ddot{q}(t)\cos\left(\frac{2\pi}{T}t - q(t)\right) - \dot{q}\sin\left(\frac{2\pi}{T}t - q(t)\right)\left(\frac{2\pi}{T} - \dot{q}(t)\right)$
q_0	$q(t = 0)$ (rad)
$M_c(t)$	CBCP input torque (N m)
$T_c(t)$	CBCP kinetic energy (J)
$M_o(t)$	original mechanism input torque (N m)
$T_o(t)$	original mechanism kinetic energy (J)
m^*	generalized mass (kg)
J_i^*	generalized moments of inertia $(\mathrm{kg\,m^2})$ ($i = \{1, 2, 3\}$)
J_{eq}	combined system equivalent inertia $(\mathrm{kg\,m^2})$
$J_{\mathrm{eq},o}(t)$	original mechanism equivalent inertia $(\mathrm{kg\,m^2})$
$f(t)$	cam follower angular position (rad)
J	follower moment of inertia w.r.t. o_5 $(\mathrm{kg\,m^2})$
R^*, d^*	radius (m) and length (m) of additional coupler cylinder

R_{c1}, R_{c2}, R_{c3}	secondary parameters defining coupler shape (m)
$d_{c1}, d_{c2}, d_{c3}, d_{c4}$	secondary parameters defining coupler shape (m)
$R_{r1}, R_{r2}, d_{r1}, d_{r2}$	secondary parameters defining rotor shape (m)
$\mathbf{p}_b$	vector of rolling body secondary parameters
$\mathbf{p}_c$	vector of coupler secondary parameters
$\mathbf{p}_r$	vector of rotor secondary parameters
Δ	safety tolerance for collision constraint (m)
i_1	collision flag no.1 (m)
i_2	collision flag no.2 (m)
$d(\cdot, \cdot)$	distance between two points (m)
$N_c(g)$	contact force between cam and rolling body (N)
$\sigma_H(g)$	Hertzian pressure in the cams (MPa)
$(\cdot)_{\max}$	$\max_{t \in [0,T]}(\cdot)$ or $\max_{g \in [0,2\pi]}(\cdot)$
$(\cdot)_{\min}$	$\min_{t \in [0,T]}(\cdot)$ or $\min_{g \in [0,2\pi]}(\cdot)$
$(\cdot)^M$	upper bound on $(\cdot)$
$(\cdot)^m$	lower bound on $(\cdot)$
L_b	lifetime of coupler-rolling body bearing (h)
L_c	lifetime of rotor-coupler bearing (h)
$r(g)$	radius of CBCP cam profile (m)
$M_s(t)$	shaking moment exerted by CBCP on mechanism frame (N m)
$g_{\mathrm{sley}}(t)$	sley axis rotation angle (rad)
$g_{\mathrm{shed}}(t)$	shed axis rotation angle (rad)
$T_{\mathrm{fly}}(t)$	flywheel kinetic energy (J)
$T_{\mathrm{sley}}(t)$	sley kinetic energy (J)
$T_{\mathrm{shed}}(t)$	shed kinetic energy (J)
J_{fly}	wheel centroidal moment of inertia $(\mathrm{kg\,m^2})$
J_{sley}	sley centroidal moment of inertia $(\mathrm{kg\,m^2})$
J_{shed}	shed mass (kg)
κ	coeffficient of drive speed fluctuation (dimensionless)

1. Introduction

This section summarizes the main theoretical results developed in the companion paper [1], as well as the characteristics of the high-speed cam-follower mechanism to be balanced.

The cam-based centrifugal pendulum (CBCP) of Fig. 1 constitutes of (i) a rotor, revolving around the ground point $\hat{o}_1$, (ii) the couplers c and c', both connected to the rotor through a revolute joint, and (iii) the rolling bodies b and b', connected to the corresponding couplers by a revolute joint. Rotation of the rotor generates centrifugal forces that push b and b' against the internal cams p and p', respectively. The cams are fixed to the mechanism frame. $g(t)$ (rad) and $q(t)$ (rad), respectively, denote the rotor's and coupler's rotation angle w.r.t. the X-axis.

The cams are designed in such a way that the input torque $M_c(t)$ (N m) required to drive (with constant speed) the CBCP is opposite to the input torque $M_o(t)$ (N m) to drive the original[1] system, such that the net input torque to drive the combined system equals zero. This is expressed by the following nonlinear, second-order, explicit, ordinary differential equation (ODE) in $q(t)$:

$$\frac{1}{2\pi/T} J_2^* \dot{q}\ddot{q} + J_3^* s + M_o(t) = 0, \tag{1}$$

where

$$s(t) = \ddot{q}\,\cos\left(\frac{2\pi}{T}t - q\right) - \dot{q}\,\sin\left(\frac{2\pi}{T}t - q\right)\left(\frac{2\pi}{T} - \dot{q}\right), \tag{2}$$

$$J_2^* = 2(J_c + m_c X_c^2 + m^* L_c^2), \tag{3}$$

$$J_3^* = 2(m_c X_c L_r + m^* L_c L_r), \tag{4}$$

$$m^* = \frac{J_b}{R_b^2} + m_b. \tag{5}$$

Even though this is a second-order ODE, it has only one independent initial condition, that is, $q(0) = q_0$. m_b (kg), J_b (kg m^2) and R_b (m), respectively, denote the mass, centroidal moment of inertia and radius of the rolling bodies. m_c (kg) and J_c (kg m^2), respectively, denote the coupler mass and centroidal moment of inertia, whereas X_c (m) determines the coupler center of mass location (see Fig. 1). $2L_r$ (m) and L_c (m), respectively, represent the rotor and coupler length. T (s) denotes the mechanism's period of motion.

Assuming that the original system is conservative, the combined system has constant energy such that it can be considered as an equivalent flywheel with inertia J_{eq} (kg m^2), turning at $2\pi/T$ (rad/s). It can be shown that J_{eq} is independent of T, provided that the original mechanism is purely inertial. In that case, its value is determined as

$$\frac{J_{eq}(2\pi/T)^2}{2} = T_o(t) + T_c(t) = T_{o,0} + T_{c,0}, \tag{6}$$

----

[1]Throughout this paper, the term *original* system will denote the mechanism to be input torque balanced, whereas the *combined system* is the ensemble of the original mechanism and the CBCP.
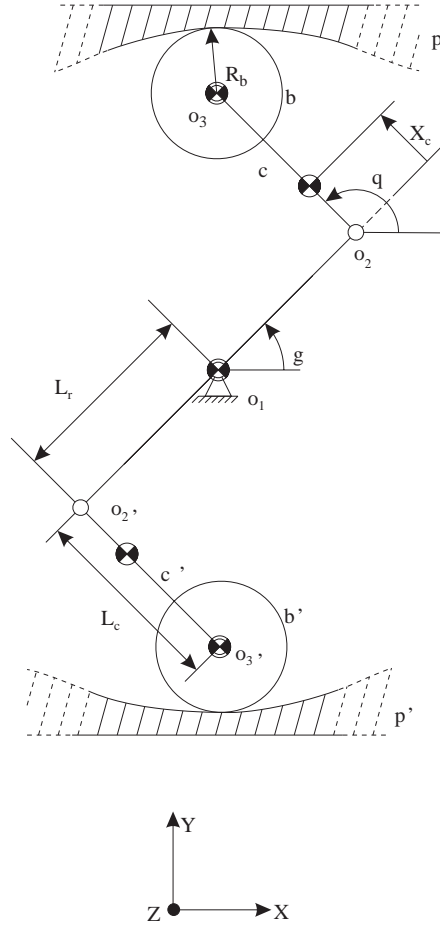
Fig. 1. Cam-based centrifugal pendulum (CBCP): kinematic scheme. The Z-axis is defined to be parallel to the drive shaft.

where $T_o(t)$ (J) and $T_c(t)$ (J), respectively, denote the original system's and the CBCP's kinetic energy. $T_c(t)$ equals

$$T_c(t) = \frac{J_1^*(2\pi/T)^2}{2} + \frac{J_2^*\dot{q}^2}{2} + J_3^*\left(\frac{2\pi}{T}\right)\dot{q}\,\cos\left(\frac{2\pi}{T}t - q\right),\tag{7}$$

where

$$J_1^* = J_r + 2(m_c L_r^2 + m^* L_r^2).\tag{8}$$

J_r (kg m^2) denotes the rotor centroidal moment of inertia.

The mechanism to be balanced is a high-speed, conjugate cam-follower system, driving the sley of a weaving loom. Its oscillating, statically balanced follower has a centroidal moment of inertia J of 0.2633 kg m^2. The mechanism's period of motion is $T = 0.0667$ s, which corresponds to an average drive speed $\omega = 2\pi/T = 94.2$ rad/s, or 900 rev/min. Fig. 2 shows one period of its desired motion f, which is a Fourier series containing six harmonics. The cam-follower system's kinetic
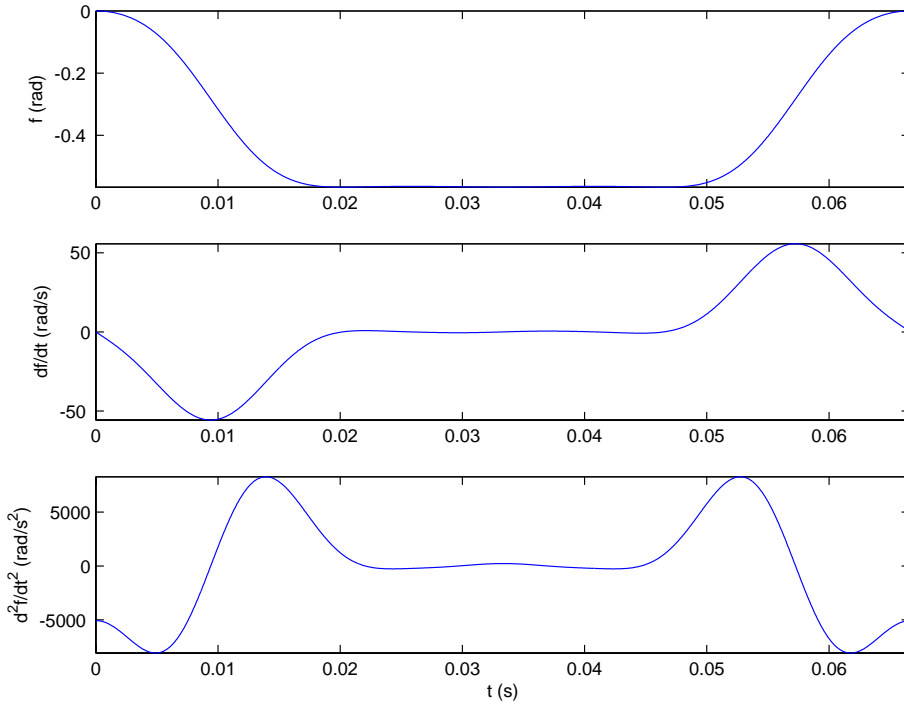
Fig. 2. Desired position, velocity and acceleration of the design example's cam follower.

energy T_o and input torque M_o equal:

$$T_o(t) = \frac{J\dot{f}^2}{2},$$ (9)

$$M_o = \frac{1}{2\pi/T}J\dot{f}\ddot{f}.$$ (10)

Combining Eqs. (9) and (7) with Eq. (6) yields

$$J_{\text{eq}} = J_1^* + \left(\frac{T}{2\pi}\right)^2 (J_2^*\dot{q}^2 + J\dot{f}^2) + \frac{T}{\pi}J_3^*\dot{q}\,\cos\left(\frac{2\pi}{T}t - q\right).$$ (11)

It was chosen to input torque balance this mechanism using two identical CBCPs. This results in smaller cams, since each CBCP has to deliver half of the required torque. Secondly, using two CBCPs allows mutual cancellation of their bending moments exerted on the drive shaft.

2. Design optimization: outline

An inspection of the describing equation (1) shows that, given the torque $M_o(t)$ to be balanced and the period of motion T, q depends on three *fundamental* parameters: J_2^*, J_3^* and the initial condition q_0. Since Eqs. (3)–(5) show J_2^* and J_3^* to depend on L_c, L_r, R_b, m_c, m_b, J_c, J_b and X_c, the following nine *design* parameters affect q and hence the shape and the technological properties of the CBCP: the kinematic parameters L_c, L_r and R_b, the mass parameters m_c, m_b, J_c, J_b and X_c and the initial condition q_0. These parameters can be determined based on an optimization problem so as to obtain a compact and technologically feasible mechanism. In the following, first of all, the optimization parameters are identified. Then, the goal function is introduced and the optimization constraints are determined. Lastly, the optimization algorithm is discussed.

2.1. Optimization parameters

The aforementioned nine design parameters could be used as the optimization parameters. However, in order to reduce the number of optimization parameters, the following assumptions are made. Firstly it is assumed that some given bearing, chosen from a catalogue, implements the revolute joint between the rolling body and the coupler. This determines m_b, J_b and R_b, since these are properties of the outer bearing ring. These parameters are grouped into the parameter vector $\mathbf{p}_b \in \mathcal{R}^3$:

$$\mathbf{p}_b = [m_b \quad J_b \quad R_b].$$

The idea is that the designer chooses the bearing, then performs the design optimization and afterwards makes a check as to whether the bearing is strong enough. If not, another bearing has to be chosen, and a new design optimization has to be done.

Secondly, m_c, J_c and X_c are replaced by one design parameter R^*, by parameterizing the shape of the coupler, as shown[2] in Fig. 3. The coupler is made up of a kind of fork, which supports the inner ring of the bearing and an additional mass. This additional mass is a cylinder with radius R^* (m) and length d^* (m).

The coupler's shape, and hence its mass parameters m_c, J_c and X_c are completely determined by the geometric parameters defined in Fig. 3: R_{c1}, R_{c2}, R_{c3}, R^*, d_{c1}, d_{c2}, d_{c3}, d_{c4}, d^* and L_c. The parameter vector $\mathbf{p}_c \in \mathcal{R}^8$ is defined as

$$\mathbf{p}_c = [R_{c1} \quad R_{c2} \quad R_{c3} \quad d^* \quad d_{c1} \quad d_{c2} \quad d_{c3} \quad d_{c4}].$$

Hence

$$m_c = m_c(L_c, R^*, \mathbf{p}_c), \tag{12}$$

$$J_c = J_c(L_c, R^*, \mathbf{p}_c), \tag{13}$$

$$X_c = X_c(L_c, R^*, \mathbf{p}_c). \tag{14}$$

---

[2] Fig. 3 is not a technical drawing of the coupler, but only defines the parameters that affect the overall shape of it.
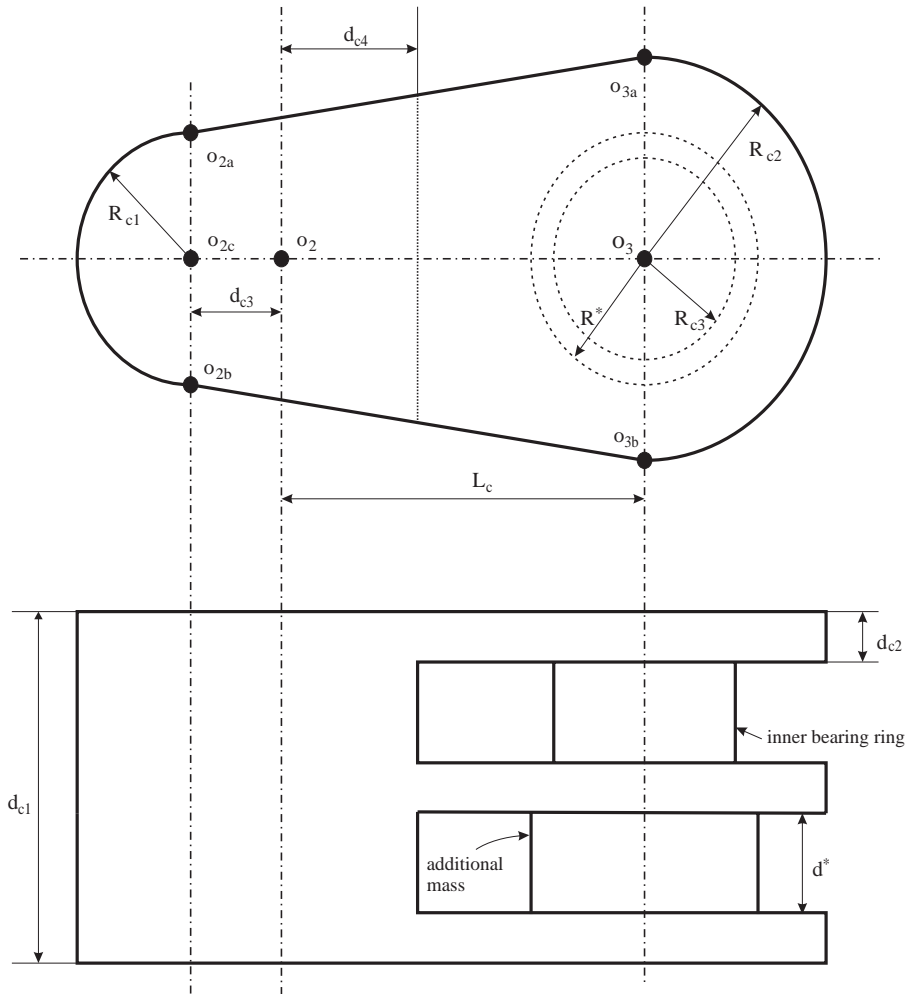
Fig. 3. Front and top view of the coupler.

Only L_c and R^* are considered for optimization whereas $\mathbf{p}_c$ is assigned a reasonable, fixed value which has to be checked after the design optimization. If the resulting coupler does not have sufficient structural strength, $\mathbf{p}_c$ has to be modified and a new optimization has to be done.

2.2. Goal function

Several criteria can be chosen for the optimization: minimal size of the cams, maximal bearing lifetime, etc. The goal function chosen here is minimal equivalent inertia J_{eq} ($\mathrm{kg\,m^2}$). The numerical value of J_{eq} is determined based on Eq. (11). The rationale for choosing J_{eq} as the optimization criterion is that inertia minimization was exactly the reason for using a torque balancing mechanism instead of a large flywheel.
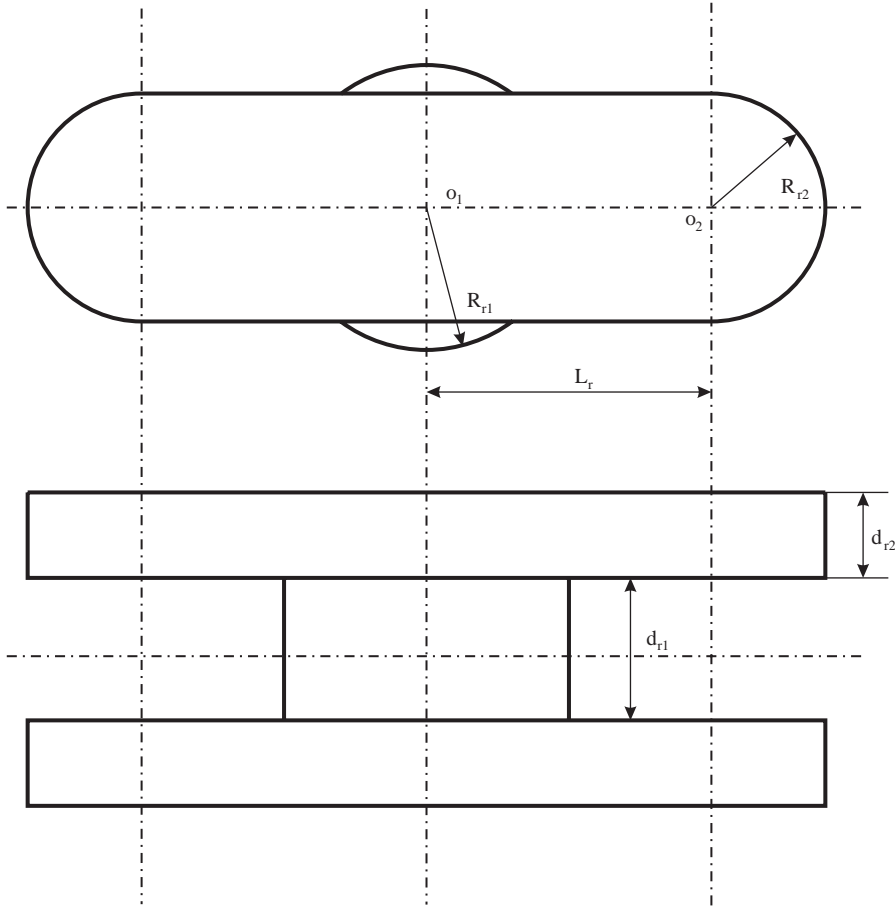
Fig. 4. Front and top view of the rotor. Parameter d_{r1} is equal to parameter d_{c1} in Fig. 3.

A practical consequence of this choice of goal function is that J_r also becomes a design parameter. J_r is, however, not considered as an optimization parameter, as it is calculated based on a parameterization of the rotor's shape shown in Fig. 4. The rotor's shape, and hence J_r are completely determined by the geometric parameters R_{r1}, R_{r2}, d_{r1}, d_{r2}, L_r. The parameter vector $\mathbf{p}_r \in \mathscr{R}^4$ is defined as

$$\mathbf{p}_r = [R_{r1} \quad R_{r2} \quad d_{r1} \quad d_{r2}].$$

Hence

$$J_r = J_r(L_r, \mathbf{p}_r). \tag{15}$$

Only L_r is considered for optimization whereas $\mathbf{p}_r$ is assigned a reasonable, fixed value. Again, this fixed value has to be checked after the design optimization. If the resulting rotor does not have sufficient structural strength, $\mathbf{p}_r$ has to be modified and a new optimization has to be done.

From the above discussion L_r, L_c, R^* and q_0 emerge as the optimization parameters. The 15 secondary parameters to which fixed values are assigned and which have to be validated after the design optimization are contained in the parameter vectors $\mathbf{p}_b \in \mathscr{R}^3$, $\mathbf{p}_c \in \mathscr{R}^8$ and $\mathbf{p}_r \in \mathscr{R}^4$.

Note that firstly, J_1^*, J_2^* and q_0 were identified to be the three *fundamental* parameters affecting Eq. (1). Then, it was shown that these three fundamental parameters depend on nine *design* parameters. Lastly, based on the rotor and coupler shape parameterization, these nine design parameters were replaced by four *optimization* parameters and 15 *secondary* parameters. One may wonder about the use of replacing the three fundamental parameters by four optimization parameters and 15 secondary parameters. This has the following advantages: (i) the rotor and coupler shape are automatically determined such that collision constraints are easily implementable (as shown hereafter) and (ii) it reflects that the bearing parameters $\mathbf{p}_b$ can only assume a discrete set of values, chosen from a catalogue.

2.3. Constraints

There are three kinds of constraints: (i) bound constraints on the optimization parameters, (ii) constraints in order to obtain a technologically feasible mechanism and (iii) constraints in order to avoid collisions between mechanism parts.

2.3.1. Bound constraints
The bound constraints on the optimization parameters take the following form:

$$L_r \geqslant L_r^m, \tag{16}$$

$$L_c \geqslant L_c^m, \tag{17}$$

$$R^* \leqslant R^{*,M}, \tag{18}$$

$$q_0 \geqslant 0. \tag{19}$$

The first two constraints express that L_r and L_c should both have a minimal length, in order to avoid construction problems. The third constraint imposes an upper bound on R^* in order to avoid excessive additional masses. The fourth constraint makes sure that only positive values of q_0 are considered since opposite values of q_0 yield an identical dynamic behavior of the mechanism. Therefore it makes sense to tighten the search space using this positivity[3] constraint.

2.3.2. Technological constraints
The following technological constraints have been taken into account. Firstly, there must always be contact between the rolling bodies and the cams. This can be mathematically expressed by imposing that the contact force $N_c(g)$ (N) between the cams and the rolling bodies should have a minimum $N_{c,\min}$ over $[0, 2\pi]$ which is greater than zero, or for robustness reasons, greater than some positive lower bound N_c^m:

$$N_{c,\min} \geqslant N_c^m. \tag{20}$$

---

[3]Imposing a negativity constraint yields identical optimization results, except for the sign of q_0 of course.

The relation between $N_{c,\min}$ and the optimization parameters is determined by establishing a classical inverse dynamic analysis. For reasons of brevity, this analysis is not included here.

Secondly, the Hertzian pressure $\sigma_H(g)$ (MPa) in the cam should have a maximum $\sigma_{H,\max}$ over $[0, 2\pi]$ which is less than some upper bound σ_H^M:

$$\sigma_{H,\max} \leqslant \sigma_H^M. \tag{21}$$

The relation between $\sigma_{H,\max}$ and the optimization parameters is based on classical formulae for Hertzian pressure in point contacts.

Thirdly, the lifetime L_b (h) of the bearing that implements the revolute joint between the rolling body and the coupler, and the lifetime L_c (h) of the bearing that implements the revolute joint between the rotor and the coupler should be greater than some minimal lifetime:

$$L_b \geqslant L_b^m,$$

$$L_c \geqslant L_c^m.$$

The relation between L_b and L_c and the optimization parameters is determined based on classical bearing lifetime formulae for which the input is generated by the inverse dynamic analysis.

2.3.3. Collision constraints

Fig. 5 shows the assembly of the rotor r, coupler c and rolling body b. When the coupler moves w.r.t. the rotor, two collisions may occur: (i) a collision between the outer bearing ring (that is, the rolling body b) and the cylinder of radius R_{r1} that belongs to the rotor and (ii) a collision between the coupler and this same cylinder.

Avoiding the first possible collision can be mathematically expressed by imposing that the distance $d(o_1, o_3)$ between o_1 and o_3 be greater than $R_{r1} + \Delta + R_b$:

$$(o_{1x} - o_{3x})^2 + (o_{1y} - o_{3y})^2 \geqslant (R_{r1} + \Delta + R_b)^2,$$

where Δ (m) represents a safety tolerance, $o_{1x} = 0$, $o_{1y} = 0$ and (see Fig. 1)

$$o_{3x} = L_r \cos(g) + L_c \cos(q),$$

$$o_{3y} = L_r \sin(g) + L_c \sin(q).$$

The circle with origin o_1 and radius $R_{r1} + \Delta$ is shown as a dash–dotted line in Fig. 5.

Avoiding the second possible collision can be expressed by the following four conditions:

- must be no intersection between the line segment $[o_{2b}\ o_{3b}]$ and the circle with origin o_1 and radius $R_{r1} + \Delta$;
- there must be no intersection between the line segment $[o_{2a}\ o_{3a}]$ and the circle with origin o_1 and radius $R_{r1} + \Delta$;
- there must be no intersection between the circle with origin o_{2c} and radius R_{c1} and the circle with origin o_1 and radius $R_{r1} + \Delta : d(o_1, o_{2c}) \geqslant R_{r1} + \Delta + R_{c1}$;
- there must be no intersection between the circle with origin o_3 and radius R_{c2} and the circle with origin o_1 and radius $R_{r1} + \Delta : d(o_1, o_3) \geqslant R_{r1} + \Delta + R_{c2}$. If $R_b \geqslant R_{c2}$, this is a redundant constraint (see the first collision constraint).
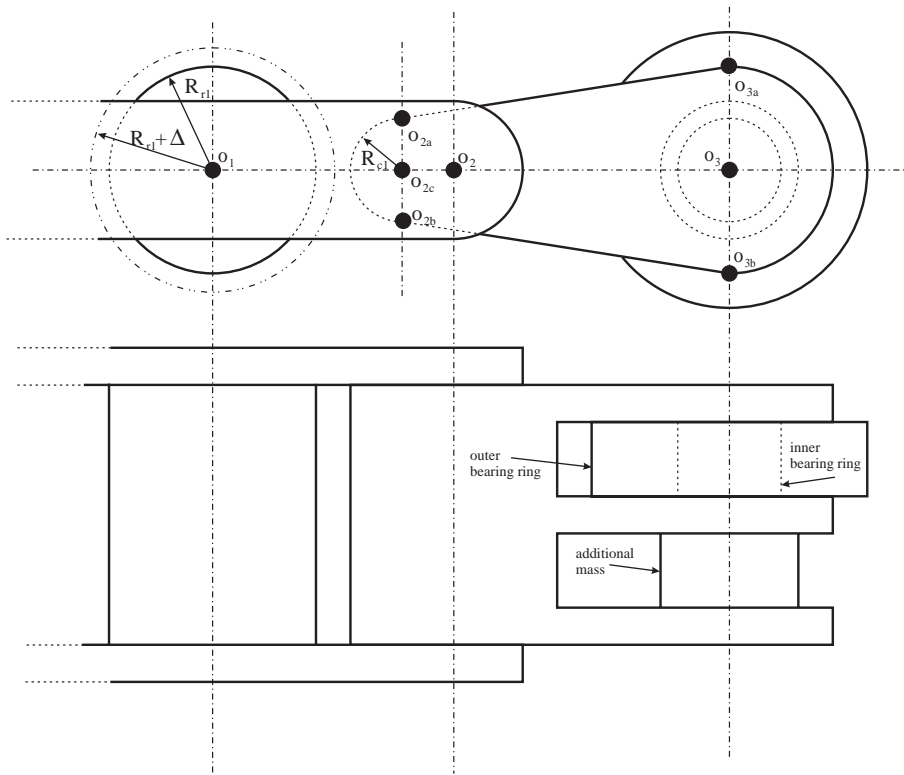
Fig. 5. Front and top view of the assembled rotor, coupler and rolling body.

The translation of these four conditions into functions of the optimization parameters is based on basic results from analytical geometry and is not included here for reasons of brevity.

In order to numerically quantify the two collision constraints, the collision flags i_1 (m) and i_2 (m) are introduced. If somewhere in the motion cycle a collision is detected, these flags are set to one. If not, they are given a negative value equal to minus the minimal (over one period of motion) distance between the respective possibly colliding bodies.

2.4. Optimization algorithm

The optimization problem with the optimization parameters, goal function and constraints outlined above is solved using the fmincon algorithm of the MATLAB OPTIMIZATION TOOLBOX. This algorithm implements a Sequential Quadratic Programming (SQP) technique.

As the optimization problem is highly nonconvex, the algorithm is likely to get stuck in local optima. The authors have therefore chosen to start the optimization from several different starting points. Afterwards, the most optimal local optimum has been chosen. Due to the optimization problem's nonconvex nature, there is no guarantee that this optimum is the global minimum. However, for this particular optimization problem, using the SQP technique with multiple starting points yielded local optima resulting in very reasonable CBCP designs. Hence,

the authors felt no need to apply more advanced global optimization techniques (such as genetic algorithms) to find a better (or the global) optimum.

3. Design optimization: results

In this section, the optimization outlined in the previous section is applied to the high-speed cam-follower system introduced in Section 1. Firstly, the optimal values of the design parameters are determined, using the multi-start SQP approach. Secondly, the optimization results are thoroughly analyzed in order to gain a better understanding of the optimization process. Finally, the possibilities for multi-criterion optimization are revealed.

3.1. SQP results

In order to optimize the design parameters L_r, L_c, R^* and q_0, knowledge is required of (i) $M_o(t)$, (ii) the secondary parameters $\mathbf{p}_b$, $\mathbf{p}_c$ and $\mathbf{p}_r$ and (iii) the parameters that define the bound, technological and collision constraints. $M_o(t)$ is calculated based on $f(t)$ and its derivatives, using Eq. (10). For the bearing that implements the revolute joint between the rolling body and the coupler, a roller bearing was chosen, whose outer ring has mass $m_b = 1.33$ kg, centroidal moment of inertia $J_b = 0.002568$ kg m^2 and radius $R_b = 0.05$ m.[4] The numerical values of $\mathbf{p}_c$ and $\mathbf{p}_r$ have been omitted for reasons of brevity. Furthermore, the following numerical values for the bound and technological constraints were used: $L_r^m = 0.072$ m, $L_c^m = 0.0792$ m, $R^{*,M} = 0.035$ m, $N_c^m = 100$ N, $\sigma_H^M = 900$ MPa, $L_b^m = L_c^m = 50,000$ h and $\Delta = 0.002$ m.

The starting points for the optimization were generated as all possible combinations of the following values:

$$L_r : \{0.08, 0.11, 0.14\} \text{ m};$$
$$L_c : \{0.08, 0.11, 0.14\} \text{ m};$$
$$q_0 : \{5.7°, 27.5°, 49.3°, 71.0°, 92.8°, 114.6°\};$$
$$R^* : \{0, 0.012, 0.023, 0.035\} \text{ m},$$

resulting in $3 \times 3 \times 6 \times 4 = 216$ different starting points for the optimization. Fifty-seven of the 216 optimizations converged to a local optimum. For the best local optimum, labelled $\mathbf{p}_1$, the first row of Table 1 summarizes the values of the optimization parameters, the goal function and the constraints. The lower bound constraint on L_r is active, together with constraints (20–21) on $N_{c,\min}$ and $\sigma_{H,\max}$. Combining $\mathbf{p}_1$ with the fixed secondary parameter values gives rise to the design parameter values of Table 1 in the companion paper [1]. Section 4.3 of Ref. [1] furthermore gives a detailed analysis of the properties of the corresponding CBCP.

---

[4]This bearing has a dynamic load capacity of $C_b = 137$ kN, whereas the bearing that implements the revolute joint between the rotor and the coupler has a dynamic load capacity C_c of 28 kN.

Table 1
Properties of the local minima p_1, p_2 and p_3. p_1 and p_2 are both obtained using the multiple-start SQP-approach

	Goal	Optimization parameters				Constraints						Secondary goals	
	J_{eq} (kg m^2)	L_r (mm)	L_c (mm)	q_0 (deg)	R^* (mm)	$N_{c,min}$ (N)	$\sigma_{H,max}$ (Mpa)	L_b (1000 h)	L_c (1000 h)	i_1 (mm)	i_2 (mm)	r_{max} (mm)	$M_{s,max}$ (N m)
p_1	0.4060	**72.0**	83.1	100.16	24.1	**100**	**900**	742	614	−9.1	−3.7	154.8	211
p_2	0.4074	**72.0**	**79.0**	94.23	21.5	**100**	890	854	619	−12.1	−5.1	157.7	199
p_3	0.4066	**72.0**	**79.0**	97.02	24.2	**100**	**900**	740	615	−9.4	−4.5	155.0	212

p_1 is the overall best local optimum, whereas p_2 is the best local optimum for which $L_r = 0.072$ and $L_c = 0.079$. p_3 is the best point obtained using the exhaustive search. Boldface values indicate active constraints.

3.2. Analysis of optimization results

In order to interpret the optimization process, firstly the active constraints for the 25 best of the total of 57 local optima were analyzed: the lower bounds (16) and (17) on L_r and L_c were, respectively, 22 and 8 times active; the lower bound (20) on $N_{c,min}$ was 17 times active, whereas the upper bound (21) on $\sigma_{H,max}$ was 5 times active. None of the other constraints were ever active.

Since the bound constraints (16–17) on L_r and L_c were, respectively, mostly or sometimes active, it was decided to do an exhaustive search in the search space obtained by setting $L_r =$ 72 mm and $L_c = 79$ mm, and choosing 30 equally spaced values for q_0 between 57° and 99°, and 40 equally spaced values for R^* between 0 and 35 mm. For these 1200 combinations of (q_0, R^*), the value of J_{eq} can be determined from Fig. 6 based on the colors defined in the colored bar next to the figure: the lowest values of J_{eq} are found in the upper left corner of the figure, while the highest values are found in the lower right corner. The various symbols (crosses, circles, etc.) mark (q_0, R^*) combinations at which constraints are active, and which are hence infeasible. As the constraints on $N_{c,min}$ and $\sigma_{H,max}$ delimit the feasible area, contour lines giving the (q_0, R^*) combinations for which $N_{c,min} = 100$ N and $\sigma_{H,max} = 900$ MPa have been added.

From Fig. 6 it is clear that $\mathbf{p}_3$, situated at the crossing of the $N_{c,min} = 100$ N and $\sigma_{H,max} = 900$ MPa contour lines, minimizes the goal function for $L_r = 72$ mm and $L_c = 79$ mm. Table 1 shows that $\mathbf{p}_3$ is only slightly less optimal than $\mathbf{p}_1$, the best overall local minimum (which has $L_c = 83.1 \geqslant 79$ mm). The exhaustive analysis thus generates a very good approximation of $\mathbf{p}_1$. When calculation time is limited, the exhaustive analysis can hence be used to generate a good CBCP design.

Besides providing a good approximate of the optimal design, Fig. 6 also explains why the multi-start SQP-approach generates many[5] local optima having comparable values of the goal function and with the constraint on $N_{c,min}$ being active: the contour line $N_{c,min} = 100$ N is quite parallel to the contour lines of J_{eq}, implying that when moving along the former contour line, the value of J_{eq} will merely change. Hence, if the SQP-algorithm generates an iterate at which the constraint on $N_{c,min}$ is active, it is likely to conclude that this iterate is a local optimum, for it observes a feasible point in which the goal function merely changes.

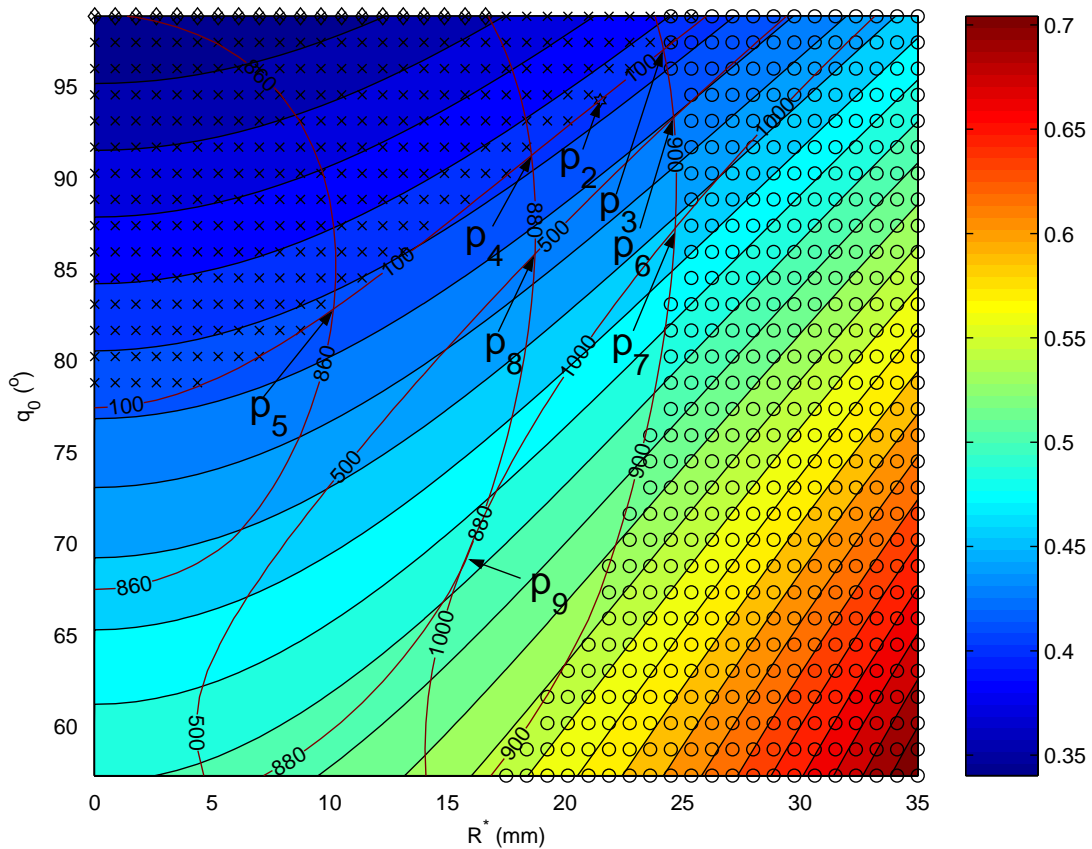[5]This is the case for 17 of the 25 best local optima.

Fig. 6. Exhaustive analysis results using J_{eq} (kg m^2) as the primary goal function. The contour lines {860, 880, 900} indicate $\sigma_{H,max}$-values (MPa). The contour lines {100, 500, 1000} indicate $N_{c,min}$-values (N). The lowest J_{eq}-values are situated in the upper left corner. The highest values are found in the lower right corner. The symbols indicate active constraints: $\times$ ($N_{c,min}$); o ($\sigma_{H,max}$); $+$ (i_1); $\diamond$ (i_2); $\triangle$ (L_b); ∇ (L_c).

Thirdly, Fig. 6 allows to assess whether $\mathbf{p}_1$ is the *global* optimum. In this figure, $\mathbf{p}_2$ is indicated, which is defined as the best point in the group of local optima (generated by the SQP-approach) that have $L_r = 72$ mm and $L_c = 79$ mm. The fact that $\mathbf{p}_2$ does not coincide with $\mathbf{p}_3$, earlier identified as the best point with $L_r = 72$ mm and $L_c = 79$ mm, suggests that the multi-start SQP-approach is not very reliable. However, the SQP-approach did find a point $\mathbf{p}_1$ that (i) is more optimal than $\mathbf{p}_3$, and (ii) like $\mathbf{p}_3$, has Eqs. (20–21) as active constraints. This indicates that there is a fair chance that $\mathbf{p}_1$ is indeed the global optimum.

Fourthly, Fig. 6 shows the sensitivity of the optimum w.r.t. the constraints. When the constraints on $N_{c,min}$ or $\sigma_{H,max}$ are changed, the new optimum is again to be found at the crossing of the corresponding contour lines. Therefore, contour lines $N_{c,min} = \{100, 500, 1000\}$ N and $\sigma_{H,max} = \{860, 880, 900\}$ MPa have been drawn in Fig. 6. From these lines, it can e.g. be learnt that keeping N_c^m equal to 100 N, while restricting σ_H^M to 880 or 860 MPa will only slightly increase the value of the goal function ($\mathbf{p}_4$ and $\mathbf{p}_5$). When on the other hand, σ_H^M is kept equal to 900 MPa, while tightening N_c^m to 500 or 1000 N, the increase of the goal function value will be somewhat

higher than in the previous case ($\mathbf{p}_6$ and $\mathbf{p}_7$). Lastly, if both constraints are tightened at the same time, the increase of the goal function will be substantial ($\mathbf{p}_8$ and $\mathbf{p}_9$).

3.3. Multi-criterion optimization

The primary goal function used so far is the value of J_{eq}. This section investigates whether it is possible to obtain a slightly worse but still reasonable value for the primary goal function, in order to obtain better values for secondary goal functions, such as r_{max} (m), the maximal radius of the cam profile or $M_{s,max}$, the maximal shaking moment. Again, some useful results are delivered by the exhaustive analysis.

Figs. 7 and 8 are built up in a similar way as Fig. 6, but now the colors indicate the value of the secondary goal functions r_{max} and $M_{s,max}$, respectively. Furthermore, the contour lines having the values 0.4280 and 0.4688 kg m^2 indicate values of the primary goal function J_{eq} that are,
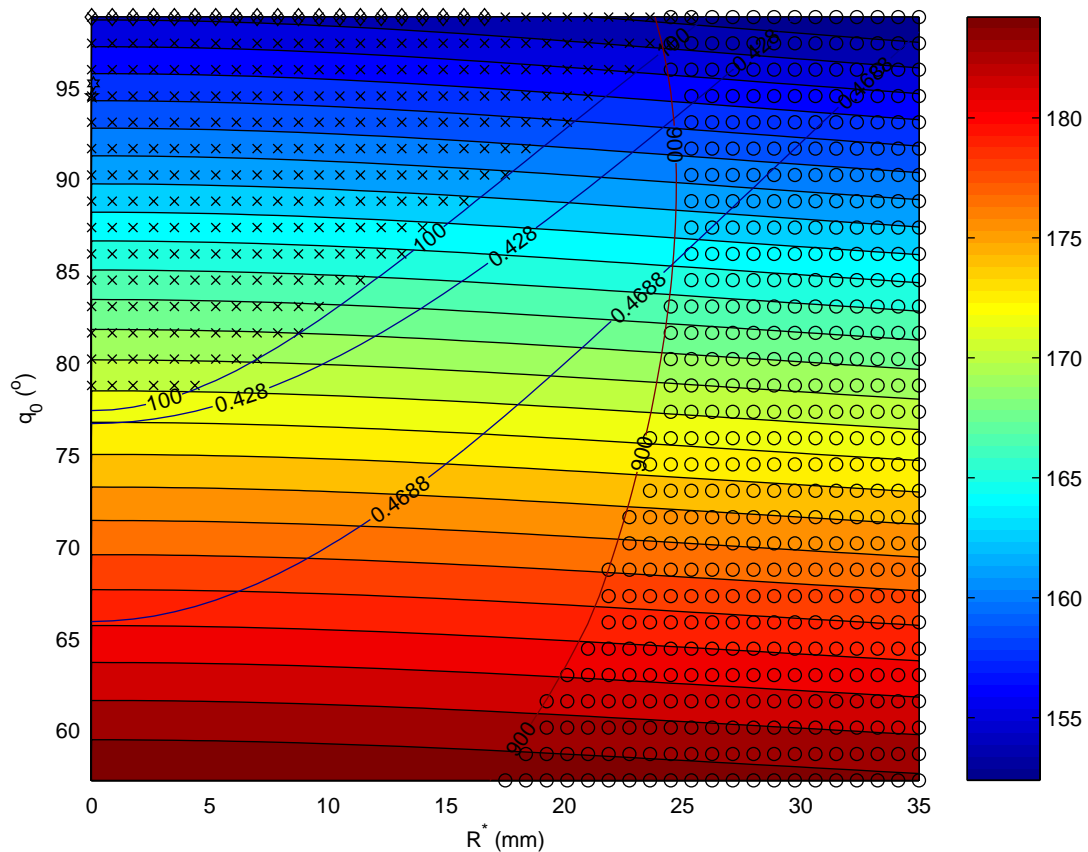

Fig. 7. Exhaustive analysis results using r_{max} (mm) as the goal function. The contour line {100} indicates the $N_{c,min} = 100$ N constraint. The contour line {900} indicates the $\sigma_{H,max} = 900$ MPa constraint. The contour lines {0.4280, 0.4688} indicate J_{eq}-values (kg m^2). The lowest r_{min}-values are situated in the upper right corner. The highest values are found in the lower left corner. The symbols indicate active constraints: $\times$ ($N_{c,min}$); o ($\sigma_{H,max}$); $+$ (i_1); $\diamond$ (i_2); $\triangle$ (L_b); ∇ (L_c).
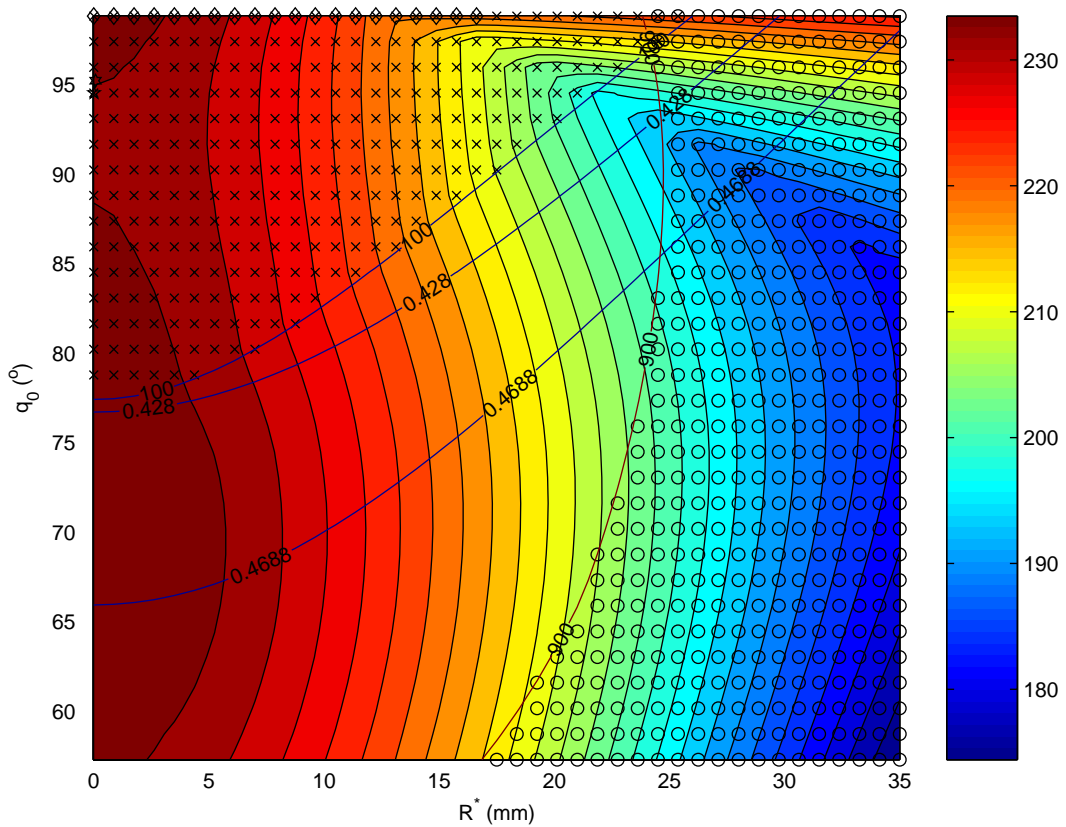
Fig. 8. Exhaustive analysis results using $M_{s,\max}$ (N m) as the goal function. The contour line {100} indicates the $N_{c,\min} = 100$ N constraint. The contour line {900} indicates the $\sigma_{H,\max} = 900$ MPa constraint. The contour lines {0.4280, 0.4688} indicate J_{eq}-values (kg m^2). The lowest $M_{s,\max}$-values are situated to the right of the figure. The highest values are found on the left. The symbols indicate active constraints: $\times$ ($N_{c,\min}$); o ($\sigma_{H,\max}$); + (i_1); $\diamond$ (i_2); $\triangle$ (L_b); ∇ (L_c).

respectively, 5% and 15% higher than the value at $\mathbf{p}_1$. Fig. 7 shows that in this case, J_{eq} and $r_{\max}$ are not competing goals, as their minimal values roughly occur in the same region. On the other hand, Fig. 8 shows that augmenting J_{eq} with 5% has the benefit of yielding a design for which $M_{s,\max}$ is somewhat lower. This optimum is situated in the neighborhood of the crossing of the $J_{eq} = 0.4280$ kg m^2 and the $\sigma_{H,\max} = 900$ MPa contour lines. On the contrary, augmenting J_{eq} with 15% does not allow a further decrease of $M_{s,\max}$.

4. Industrial case study: torque balancing a weaving loom

Airjet weaving looms are characterized by two main motions: the back-and-forth motion of the *sley* and the up-and-down motion of the *sheds*. In general, both motions are realized through cam mechanisms which convert the rotary motion of the driving motor into the desired oscillating movement. Cam mechanisms are a natural choice in this setting as they provide sufficient stiffness and robustness for these high-speed machines (drive speeds up to 1200 rev/min).

As both cam-follower mechanisms are coupled to the same main shaft, they interact dynamically. It has been observed experimentally that these interactions result in premature failure of the sheds. This can be explained by the drive speed fluctuations caused by the sley motion. As the shed cams are designed with a constant drive speed in mind, the drive speed fluctuation causes the shed motion to be distorted. This distortion results in undesired higher harmonics in the shed acceleration. The forces proportional to these undesired harmonics have been observed experimentally to excite structural shed resonances, causing excessive vibration, wear and premature failure.

Undesired harmonics are also present in the sley motion (due to the drive speed fluctuation caused by the shed motion), but these do not result in sley failure. The main designer's task for this particular case is hence to remove the undesired harmonics from the shed motion. Possible approaches include reducing the drive speed fluctuation through a large flywheel, or by using an advanced control system imposing a nearly constant drive speed. The former solution, however, compromises the start/stop behavior of the weaving loom, while the latter is too energy consuming. An intermediate solution, yielding a much more constant drive speed while keeping inertia addition within acceptable limits, is input torque balancing.

Only the sley movement was chosen to be input torque balanced. There is a double motivation for this. Firstly, both the synchronization between the sley and the shed motion and the shed inertia may vary, depending on the tissue to be fabricated. Hence, the joint input torque to be balanced is also variable, necessitating the use of separate CBCP cams for every possible synchronization and shed inertia. Secondly, the more severe problem is the effect of the sley on the shed motion. Therefore, it makes sense to concentrate on input torque balancing the sley. It will be shown in Section 4.2 that this indeed is a valid approach.

Assessment of the result of the torque balancing requires determining the regime behavior of the weaving loom. The classical way for doing so is time integrating the dynamic equations. Here, a novel approach is introduced, that is, determining the system regime behavior directly in the frequency domain. This approach is believed to be novel in mechanism literature, and is the subject of Section 4.1.

4.1. Frequency domain determination of weaving loom regime behavior

Fig. 9 shows a simplified weaving loom model, consisting of the sley and shed conjugate cam-follower systems, a flywheel J_{fly} of $0.7385\,\mathrm{kg\,m^2}$, and a CBCP. The CBCP's rotor is mounted on the sley axis, while the internal cams are fixed to the machine frame. g_{sley} and g_{shed} denote the rotation angle of the sley and shed axis, respectively. The gear pair imposes a 1:2 reduction: $\dot{g}_{\mathrm{shed}} = \dot{g}_{\mathrm{sley}}/2$.

The sley conjugate cam-follower system was introduced in Section 1. The ensemble of the sheds is considered here as the (single) translating cam-follower of a conjugate cam-follower pair. Its mass J_{shed} equals 52 kg, while its desired motion f_{shed} (m) is given in Fig. 10. Note that the overall machine period T is determined by the slowest turning axis, that is, the shed axis. Hence, $T = 2\pi/\mathrm{mean}\,(\dot{g}_{\mathrm{shed}})$. As the mean sley axis speed equals 900 rev/min, T equals 0.1333 s.

As in the companion paper [1], the simplified model is assumed to be purely inertial and hence conservative. Therefore, its resulting motion (that is, $g_{\mathrm{sley}}, g_{\mathrm{shed}}, f_{\mathrm{sley}}, f_{\mathrm{shed}}$ and their derivatives)
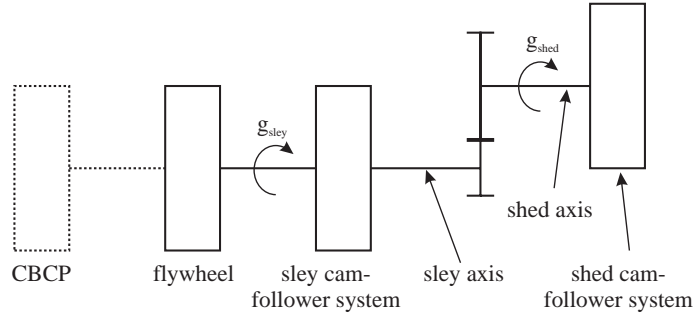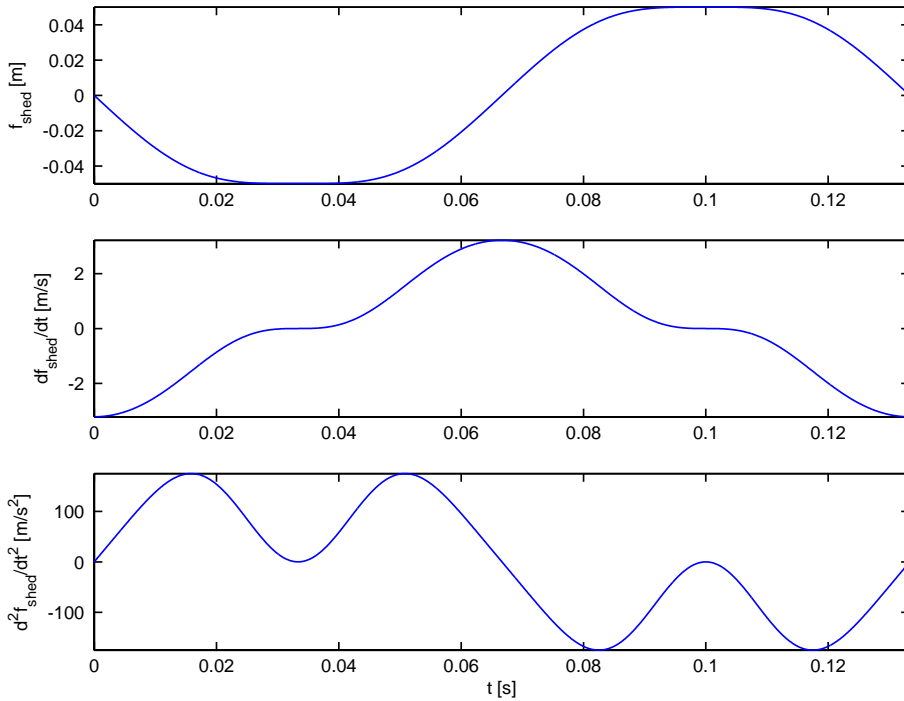
Fig. 9. Simplified weaving loom model.

Fig. 10. Shed desired motion f_{shed} and its derivatives.

can be determined by applying the principle of conservation of kinetic energy:

$$T_c(t) + T_{\text{fly}}(t) + T_{\text{sley}}(t) + T_{\text{shed}}(t) = T_{c,0} + T_{\text{fly},0} + T_{\text{sley},0} + T_{\text{shed},0}, \tag{22}$$

where $T_c(t)$, $T_{\text{fly}}(t)$, $T_{\text{sley}}(t)$ and $T_{\text{shed}}(t)$ denote the kinetic energy (J) of the CBCP, flywheel, sley and sheds, respectively, and equal:

$$T_c(t) = \frac{J_1^* \dot{g}_{\text{sley}}^2}{2} + \frac{J_2^* \dot{q}^2}{2} + J_3^* \dot{g}_{\text{sley}} \dot{q} \, \cos(g_{sley} - q), \tag{23}$$

$$T_{\text{fly}}(t) = \frac{J_{\text{fly}}\dot{g}_{\text{sley}}^2}{2}, \tag{24}$$

$$T_{\text{sley}}(t) = \frac{J_{\text{sley}}\dot{f}_{\text{sley}}^2}{2}, \tag{25}$$

$$T_{\text{shed}}(t) = \frac{J_{\text{shed}}\dot{f}_{\text{shed}}^2}{2}. \tag{26}$$

Using a concept well known in mechanism literature, that is, the concept of a motion law, it is straightforward to show that q, $\dot{q}$, $\dot{f}_{\text{sley}}$ and $\dot{f}_{\text{shed}}$ depend on g_{sley} and $\dot{g}_{\text{sley}}$. As a consequence, Eq. (22) constitutes a first-order, nonlinear, ordinary differential equation in g_{sley}. Without loss of generality, it may be assumed that the sole initial condition for this first-order ODE is $g_{\text{sley}}(0) = 0$.

In order to solve Eq. (22), an approach similar to the nonlinear least-squares approach outlined in the companion paper [1] is adopted. That is, $\dot{g}_{\text{sley}}$ is parameterized as a finite Fourier series of periodicity T, with $K = 20$ harmonics and average value $2 \times 2\pi/T$. The unknown Fourier coefficients are determined by minimizing in the least-squares sense a residual function based on Eq. (22). This nonlinear least-squares approach boils down to determining $\dot{g}_{\text{sley}}$ in the frequency domain, as the Fourier coefficients are determined directly without explicit time integration. It has the advantage of (i) direct calculation of the regime behavior and (ii) guaranteeing a solution $\dot{g}_{\text{sley}}$ with the correct periodicity (or equivalently, the right average speed).

This frequency domain approach is believed to be novel in mechanism literature. Most often, it is assumed that a mechanism is driven with constant drive speed, and hence abstraction is made of the dynamics of the drive system. The few researchers who do take the drive system dynamics into account all use a time domain approach, that is, they directly integrate the governing nonlinear differential equations to determine the steady-state mechanism behavior. The assumption of a conservative system is frequently used in German literature, see e.g. Ref. [2]. In that case, the resulting motion of the mechanism is called an *Eigenbewegung* (eigenmotion). Other authors assume that some actuator drives the system. Either a full model of the driving actuator is considered [3–6], or the actuator is modelled by an assumed torque–speed relationship, such as a motor torque which varies linearly with speed [7] or a quadratic relationship [8,9].

4.2. The effect of torque balancing

In order to assess the torque balancing effect, three different situations are compared:

(S1) original weaving loom,
(S2) original weaving loom with enlarged flywheel, and
(S3) original weaving loom with CBCP.

The CBCP added in situation (S3) is the double CBCP designed based on the optimum $\mathbf{p}_1$ determined in Section 3.1. Its rotor is mounted on the sley axis, as shown in Fig. 9. The amount of additional flywheel inertia in situation (S2) equals

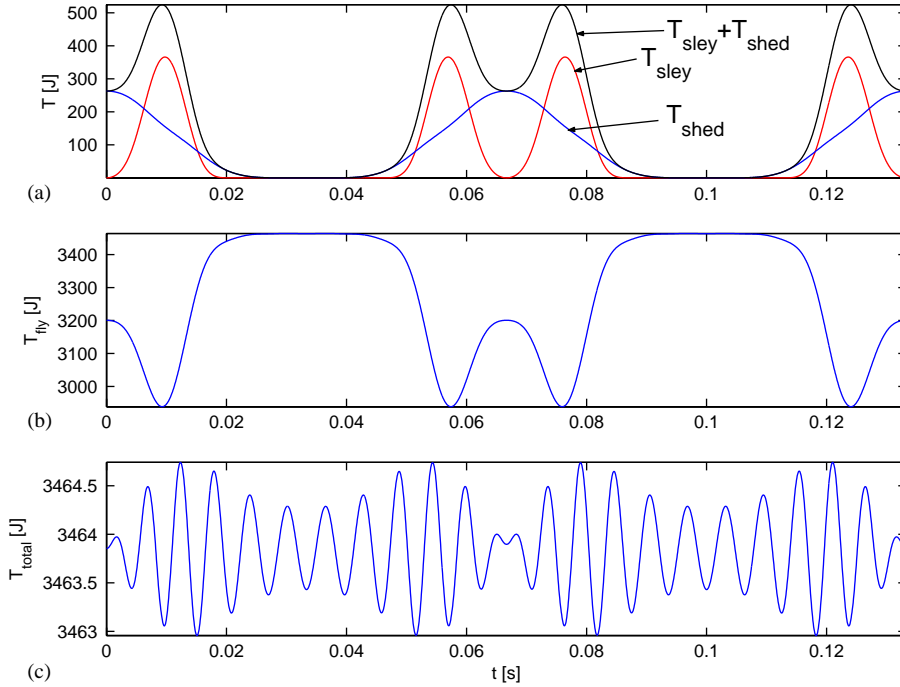$$J_{\text{eq}} - \min_{t \in [0, T_{\text{sley}}]} J_{\text{eq},o} = 0.4060 - 0.0919 = 0.3141 \text{ kg m}^2.$$

Fig. 11. Kinetic energy results for (S1): (a) T_{sley}, T_{shed} and their sum; (b) T_{fly}; (c) total kinetic energy.

This additional inertia physically implements the excess[6] part of the equivalent flywheel. In this manner, one can distinguish between the *flywheel effect* of the CBCP (the added excess, dumb inertia of $0.3141\,kg\,m^2$) and the *torque balancing effect* of the CBCP (due to its moving masses), by comparing situations (S2) and (S3).

In order to assess the difference between a machine with and without CBCP, Figs. 11 and 12 show one shed period of the kinetic energy components for (S1) and (S3). In the original machine, the sum of the sley and shed kinetic energy attains its minimum, zero, when both the sley and the sheds stand still. As a consequence, $T_{fly}(t)$, shown in Fig. 11(b) (and hence $\dot{g}_{sley}(t)$) attains its maximum of 3464 J (96.9 rad/s) in these portions of the motion cycle. When the sley and the sheds move, they withdraw kinetic energy from the flywheel, resulting in a slowdown of the latter, popping up as $T_{fly}(t)$ dips in Fig. 11(b). One clearly recognizes the four[7] sharp dips, due to the sley movement, superposed on two broader dips due to the shed movement. As a check of the solution, Fig. 11(c) shows the sum of the flywheel, sley and shed kinetic energy, which is constant, apart from some remaining jitter due to the fact that the $\dot{g}_{sley}(t)$ parameterization is truncated after 20 harmonics.

The purpose of the CBCP is to cancel out the effect of the sley motion. It is designed in such a way that the sum of $T_{sley}(t)$ and $T_c(t)$ is constant, under the assumption of $\dot{g}_{sley}(t)$ being perfectly

---

[6]that is, the excess part w.r.t. the physical lower limit $\min_{t\in[0,T_{sley}]}J_{eq,o}(t) = 0.0919\,kg\,m^2$ derived in the companion paper.

[7]During one shed period, the sley moves back and forth two times as its drive shaft has twice the speed of the shed drive shaft.
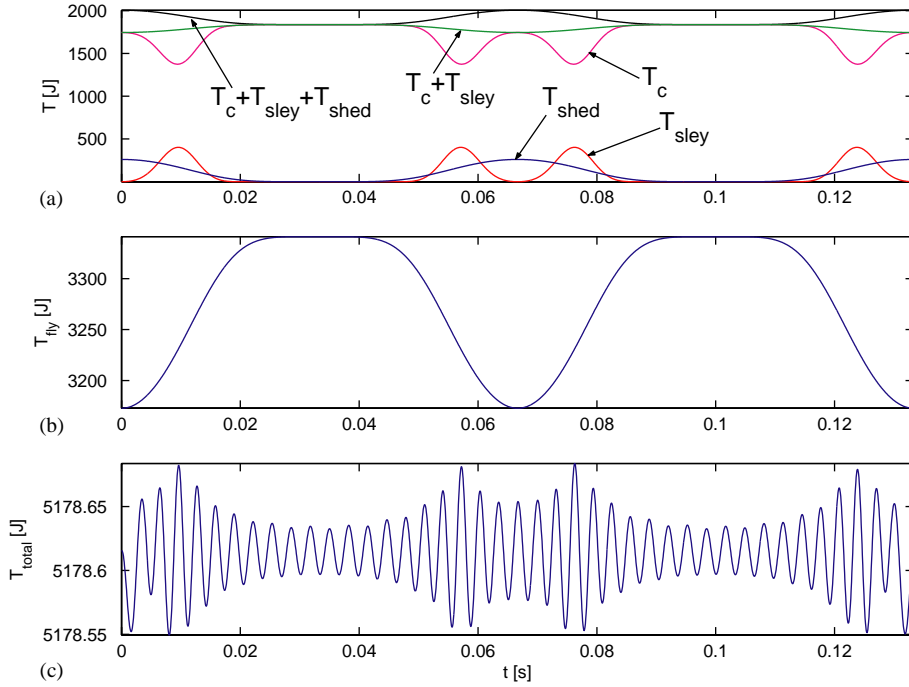
Fig. 12. Kinetic energy results for (S3): (a) T_{sley}, T_{shed}, T_c, $T_c + T_{sley}$ and $T_c + T_{sley} + T_{shed}$; (b) T_{fly}; (c) total kinetic energy.

constant. As the shed motion is not taken into account during the CBCP design, the weaving loom with CBCP will not have constant $\dot{g}_{sley}(t)$. Consequently, the sum of $T_{sley}(t)$ and $T_c(t)$ is not perfectly constant, as shown in Fig. 12(a). Still, the effect of the CBCP is clearly visible, as the sum of $T_{sley}(t)$, $T_{shed}(t)$ and $T_c(t)$ no longer exhibits four but two peaks: the effect of the sley is compensated for by the CBCP. As a result, $T_{fly}(t)$ still has two broad dips due to the (noncompensated) shed motion, whereas the sharp sley-dips have disappeared.

Based on the above discussion, an intuitive interpretation of Fig. 13, showing $\dot{g}_{sley}$ and $\ddot{g}_{sley}$ for (S1)–(S3) is straightforward. Because of Eq. (24), in Fig. 13(a), the same qualitative behavior is to be expected as in Figs. 11(b) and 12(b): in the noncompensated situations (S1) and (S2), $\dot{g}$ exhibits four sharp sley and two broad shed dips (which are of course less deep in (S2) due to the larger flywheel), while it exhibits only two broad shed dips if the CBCP is present. As a consequence, the combined system has a much smoother $\ddot{g}_{sley}$ time trajectory.

A smoother drive shaft speed fluctuation results in much smoother sley and shed acceleration trajectories as shown in Fig. 14. For (S1)–(S3), Figs. 14(a) and (c), respectively, show the actually realized sley and shed acceleration $\ddot{f}_{sley,act}$ and $\ddot{f}_{shed,act}$, whereas Figs. 14(b) and (d) show the difference $\Delta \ddot{f}_{sley}$ and $\Delta \ddot{f}_{shed}$ between the actually realized accelerations and the desired[8] acceleration. For the sley motion, the CBCP roughly seems to have a similar effect as flywheel addition: $\Delta \ddot{f}_{sley}$ exhibits the same qualitative behavior for (S1)–(S3), that is, the same peaks, but

---

[8]The desired acceleration trajectories are shown in Fig. 2(c) (sley motion) and Fig. 10(c) (shed motion).
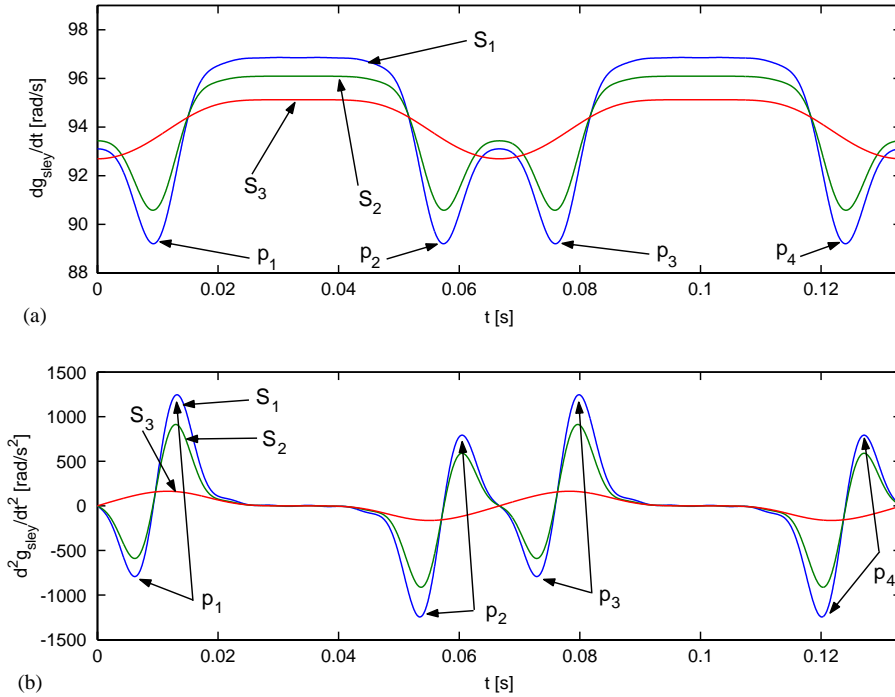
Fig. 13. Drive shaft speed (a) and acceleration (b) for situations (S1)–(S3).

with smaller amplitudes. The shed acceleration on the other hand is much more affected by the CBCP addition (which is logical: the CBCP is designed to cancel out the effect of the sley on the shed motion): also the qualitative behavior changes, since the double peaks labelled p_i, $i = \{1, 2, 3, 4\}$ in Fig. 14(d) completely disappear if the CBCP is present. An intuitive explanation for this is that the CBCP removes the four sharp double peaks labelled p_i, $i = \{1, 2, 3, 4\}$ from $\ddot{g}_{\text{sley}}$ (see Fig. 13(b)). These double peaks correspond to the four dips in $\dot{g}_{\text{sley}}$ shown in Fig. 13(a).

The sley and shed acceleration distortion has an important effect on the harmonic content of these motions. This is shown in the bar plots of Figs. 15 and 16. The shed motion law is designed to have a first, third and fifth harmonic. However, in situation (S1) and (S2), the harmonics 7, 9, 13 and 15 are clearly present. These harmonics (that is, the corresponding proportional forces and torques) are detrimental as they excite shed resonances which result in premature shed failure. In this respect, the beneficial effect of the CBCP becomes apparent: all undesired harmonics are at least 30 dB (that is, a factor 32) smaller than in the situation with enlarged flywheel (S2).

The beneficial CBCP effect is, however, not confined to the shed motion alone. The sley motion is designed to have six harmonics. Fig. 15, however, clearly indicates the presence of a seventh, eight, and ninth harmonic in situations (S1) and (S2). On the other hand, when the CBCP is present, the undesired seventh harmonic is still present (and even somewhat higher), but the eight and ninth harmonic are 30 dB (that is, a factor 32) lower. Hence, although the time domain
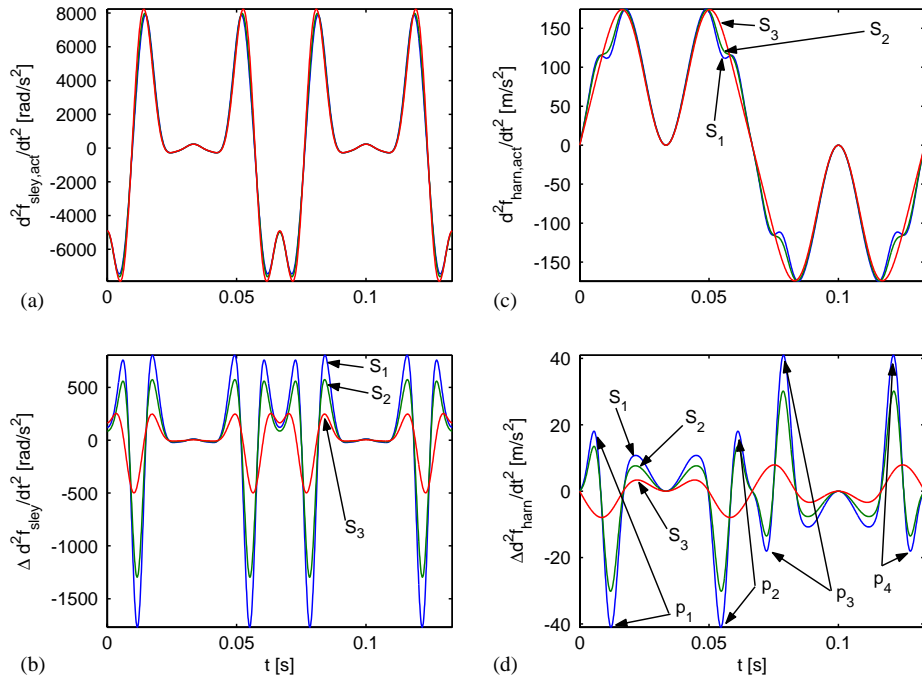
Fig. 14. Actually realized sley (a) and shed (c) acceleration and difference with the desired sley (b) and shed (d) acceleration for situations (S1)–(S3).

acceleration results suggest that the CBCP roughly has the effect of a flywheel for the sley motion, the frequency domain results prove that this is not quite true.

From this section, some important conclusions can be drawn. Firstly, it has clearly been demonstrated that mere flywheel addition cannot change the qualitative behavior of the drive speed fluctuation, as can torque balancing. Secondly, it has been shown (S1,S2) that drive speed fluctuations can have a dramatic effect on the follower acceleration. In this respect, attention must be drawn to the fact that the shape rather than the amount of drive speed fluctuation is important: in (S1), the coefficient of drive speed fluctuation κ, defined as

$$\kappa = \frac{\dot{g}_{\text{sley,max}} - \dot{g}_{\text{sley,min}}}{\dot{g}_{\text{sley,ave}}},$$

equals 8.1%, whereas it, respectively, equals 5.8% and 2.6% for (S2) and (S3). Despite the fact that the difference between κ(S2) and κ(S3) is not much larger than the difference between κ(S1) and κ(S2), the difference in acceleration distortion is much more significant, clearly illustrating the importance of the shape of the drive speed fluctuation. Thirdly, it has been shown that torque balancing is capable of yielding a dramatic decrease of the undesired acceleration harmonics. Fourthly, it is able to do so quite robustly as the decrease of the undesired acceleration harmonics is realized despite the presence of the shed mechanism, which is not taken into consideration during the CBCP design.
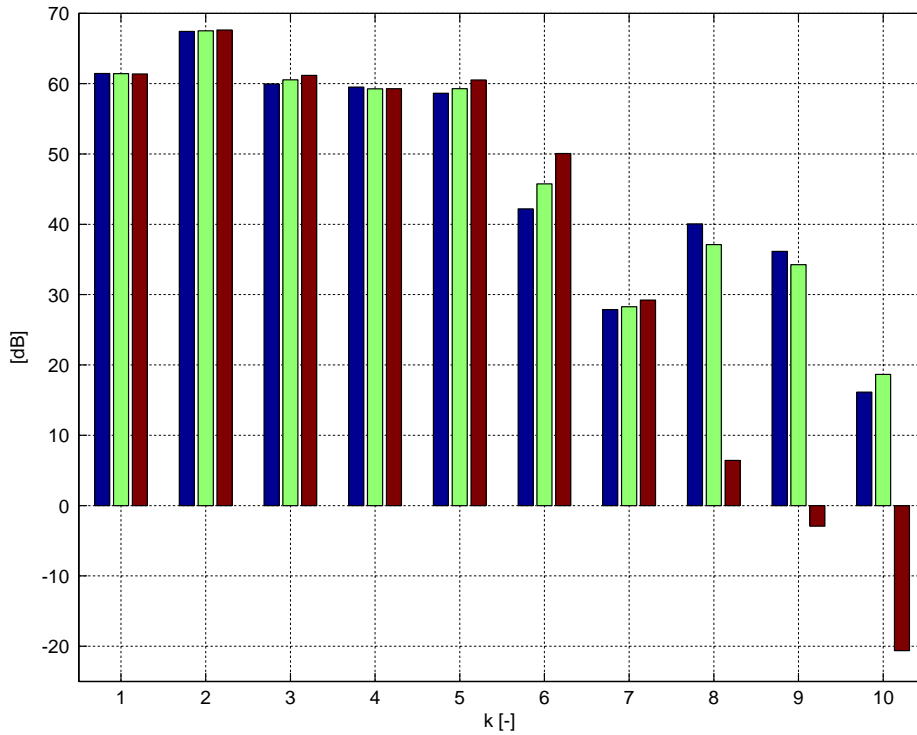
Fig. 15. Sley acceleration harmonics for situations (S1)–(S3). k denotes the harmonic order.

5. Conclusion

Nine design parameters determine the design of a CBCP. However, parameterizing the shape of the coupler and the rotor and choosing some bearing for the revolute joint between the coupler and the rolling body results in replacement of these nine parameters by (i) four optimization parameters L_r, L_c, R^* and q_0 and (ii) 15 secondary parameters, grouped into the parameter vectors $\mathbf{p}_b$, $\mathbf{p}_r$ and $\mathbf{p}_c$, and to which fixed, reasonable values are assigned. The purpose of the optimization problem is to minimize the combined system's equivalent inertia, taking into account bound, collision and technological constraints.

Application of the CBCP to torque balance a high-speed, purely inertial cam-follower mechanism illustrates that the multi-start SQP-approach results in a compact and technologically feasible mechanism. A thorough analysis of the optimization process, based on an exhaustive analysis (i) shows that the exhaustive analysis gives a good approximation of the best optimum, (ii) explains why many optima having comparable values of the goal function and an active $N_{c,\min} \geqslant 100\,\mathrm{N}$ constraint, (iii) suggests that the best optimum might be the global optimum, (iv) illustrates the sensitivity of the optimum w.r.t. the values defining the constraints and (v) reveals the possibilities for multi-criterion optimization.

Much of this research was motivated by the industrial example of the sley and shed motion in a weaving loom, which are dramatically affected by drive speed fluctuations. Determination of the
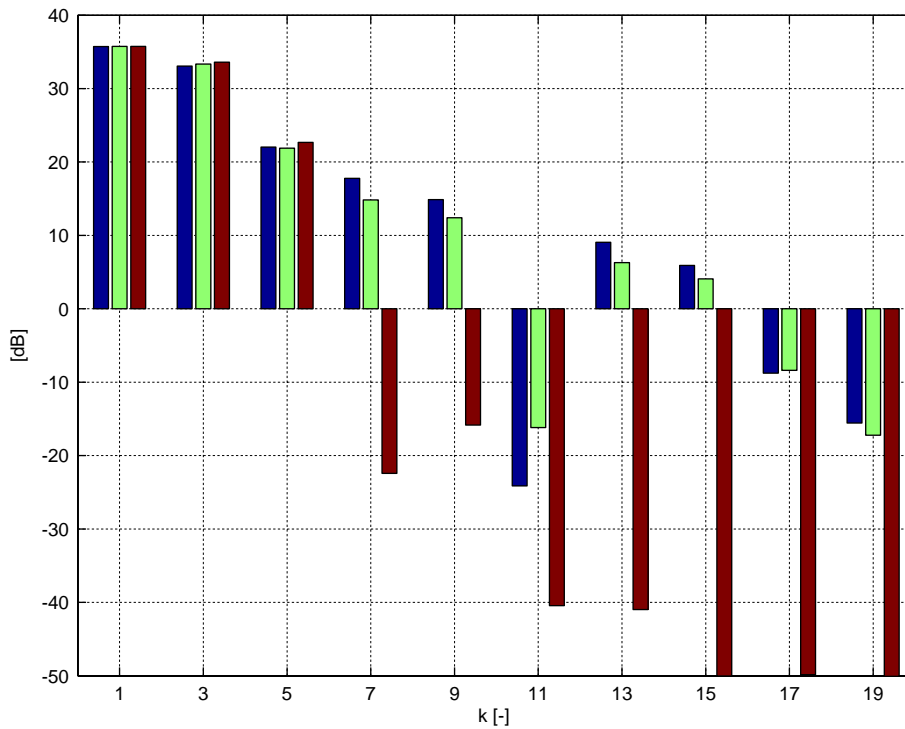
Fig. 16. Shed acceleration harmonics for situations (S1)–(S3). k denotes the harmonic order.

weaving loom regime behavior is done in the frequency domain, an approach which is believed to be novel in mechanism literature.

The CBCP has been shown (i) to have a much more significant effect on the drive speed fluctuation than mere flywheel addition, and (ii) to result in a dramatic reduction of the undesired acceleration harmonics, which are believed to be a major cause of dynamic problems of weaving looms. This example furthermore illustrates that the shape, rather than the amount of drive speed fluctuation is of concern for avoiding dynamic problems. Lastly, and most importantly, this example has shown that adding a CBCP is a robust solution, as the decrease of the undesired acceleration harmonics is realized despite the presence of the shed mechanism, not taken into consideration during the CBCP design.

Future work will mainly focus on building a CBCP prototype in order to experimentally validate its promising features.

Acknowledgements

References

[1] B. Demeulenaere, P. Spaepen, J. De Schutter, Input torque balancing using a cam-based centrifugal pendulum: design procedure and example, *Journal of Sound and Vibration* 283 (1 + 2) (2005) 1–20, this issue; doi:10.1016/j.jsv.2004.03.029.

[2] H. Dresig, *Schwingungen Mechanischer Antriebssysteme: Modellbildung, Berechnung, Analyse, Synthese* (*Vibrations of Mechanical Drive Systems: Modelling, Calculation, Analysis, Synthesis*), Springer, Berlin, 2001.

[3] J. Sadler, R. Mayne, K. Fan, Generalized study of crank–rocker mechanisms driven by a d.c. motor part i. mathematical model, *Mechanism and Machine Theory* 15 (1980) 435–445.

[4] R. Mayne, J. Sadler, K. Fan, Generalized study of crank–rocker mechanisms driven by a d.c. motor part ii. applications, *Mechanism and Machine Theory* 15 (1980) 447–461.

[5] A. Myklebust, Dynamic response of an electric motor-linkage system during startup, *Journal of Mechanical Design* 104 (1982) 137–142.

[6] F. Liou, A. Erdman, C. Lin, Dynamic analysis of a motor-gear-mechanism system, *Mechanism and Machine Theory* 26 (3) (1991) 239–252.

[7] P. Kulitzscher, Leistungsausgleich von Koppelgetrieben durch Veränderung der Massenverteilung oder Zusatzkoppelgetriebe, *Maschinenbautechnik* 19 (11) (1970) 562–568.

[8] A. Liniecki, The equation of a variable transmission ratio for a mechanical system with fluctuating load, *Journal of Mechanisms* 4 (1969) 139–144.

[9] J. Wiederrich, Analysis of drive shaft speed variations in a scotch yoke mechanism, *Journal of Mechanical Design* 104 (1982) 239–246.